ICARUS 50, 245–258 (1982)

# Photoclinometric Determination of the Topography of the Martian North Polar Cap[1]

ALAN D. HOWARD

*Department of Environmental Sciences, University of Virginia, Charlottesville, Virginia 22903*

AND

KARL R. BLASIUS AND JAMES A. CUTTS

*Planetary Science Institute, Science Applications, Inc., 283 S. Lake, Suite 218, Pasadena, California 91101*

Received July 16, 1981; revised March 3, 1982

Photoclinometry is useful for the determination of topography for areas which have a uniform albedo. The technique is applied to early spring Viking images of the Martian north polar cap, taken when the surface was covered by a nearly uniform frost cover. Unlike earlier approaches, the topographic profiling can be used for surfaces with any photometric function, but the strike of the planetary surface relative to the illumination angle must be specified along the profile. The resultant profiles are relatively insensitive to misestimation of the photometric function and slope orientation, but are quite sensitive to the assumed values of the reflectance of an equivalent level surface and the atmospheric opacity (if it is large).

## INTRODUCTION

Information concerning the topography of the Martian polar terrains is crucial for understanding the origin of the permanent ice cap, layered deposits, and vast sand seas, all features critical to deciphering the recent climatic history of the planet. The topographic relief on the cap and layered deposits is muted, with slopes seldom exceeding 5° (Dzurisin and Blasius, 1975), but slight differences in gradient and azimuth seem to determine whether or not slopes become defrosted during the polar summer season, which in turn may control whether there is net yearly ablation or deposition (Howard, 1978). The most intriguing feature of the residual summer cap is the ubiquitous, regular layering exposed on steeper defrosted slopes. The layers have been interpreted as resulting from cyclical accumulation of ice and dust controlled by climate fluctuations induced by planetary orbital variations (Cutts, 1973; Ward *et al.* 1974; Toon *et al* 1980). Determination of the total thickness and detailed stratigraphy of the layers is therefore critical for understanding the link between climate and surface processes to astronomical forcing.

Unfortunately, topographic information has been difficult to obtain for the Martian polar regions. The orbits of the Mariner 9 and Viking 2 spacecraft were nearly ideal for acquiring stereo images. The earlier mission suffered from long periods of high atmospheric opacity and a viewing geometry which limited the usefulness of the data. Medium-resolution stereo imaging just adequate to resolve outcropping layers was acquired for the region of the south polar residual cap. In the north polar region a lesser quantity of much lower-resolution stereo imaging was acquired. These data have been partially reduced (Dzurisin and Blasius, 1975). The Viking 2 Orbiter was able to acquire the best-resolution images of po-

[1] Presented at the "Workshop on Quasi-Periodic Climatic Changes on Earth and Mars" held at NASA's Ames Research Center, Moffett Field, California, February 24–26, 1981.



0019-1035/82/050245-14$02.00/0

lar terrains thus far under better atmospheric clarity conditions and over a longer period of time than Mariner 9. These data include stereo imaging of a few percent of the north residual cap under summer conditions of partial defrosting and spring conditions of total frost cover. Because of cost limitations, stereo photogrammetric analysis to date has been very limited (Blasius *et al* 1982), but a less costly alternative for topographic mapping is photoclinometry.

Photoclinometric techniques are an alternative and supplement to photogrammetric mapping, offering the advantages of lower cost and horizontal resolution limited only by the picture resolution. In addition, the technique requires only single-image coverage of the target area. Because angles of illumination of polar areas are extremely shallow, vertical resolution is good. Unfortunately, the photoclinometric technique also has potential limitations, as will be discussed later, which means that it is best suited to be used to determine relative gradients unless it can be calibrated with photogrammetric data, at least locally. Comparison of results of the two types of analysis, a necessary preface to calibration, has yielded encouraging results and is discussed in a companion paper (Blasius *et al.*, 1982).

The brightness of a surface as observed by a camera such as that on the Viking Orbiters depends upon lighting and viewing geometry, the gradient and azimuth of the slope, the photometric function of the surface, the albedo of the surface, and atmospheric absorption and scattering. Photoclinometry should be a useful technique for determining slope gradients and topographic profiles under conditions where the effects of the other variables named above can be accurately modeled (Bonner and Schmall, 1973). Applications of this technique have met with very limited success, however, due to areal variations in albedo which cannot be modeled in terms of known parameters. Squyres (1981) utilized an approach similar to the one outlined below to obtain topographic profiles on Ganymede.

The polar caps of Mars in early spring may be a nearly ideal situation for application of photometric techniques because a cover of annual frost blankets all terrain. Viking imaging of most of the north polar region was taken under these conditions. Furthermore, some stereo imaging acquired during this season is available to check the validity of photoclinometric analysis, including the assumption of uniform albedo (Blasius *et al.*, 1982). Later in the spring and summer partial defrosting made photoclinometry impossible. Here we outline a photometric topographic profiling procedure which was developed for use with photometrically corrected digital images of the Martian north polar cap taken in the early spring season (Viking 2 orbits 494–566).

NOTATION

| | |
|---|---|
| $x$, $y$ | Coordinate system on level planetary surface, $y$ axis to north, origin at optic axis intercept on planet (Fig. 1B). |
| $x'$, $y'$ | Coordinate system on image (Fig. 1A). |
| $I$, $J$ | Pixel coordinates on image (Fig. 1A). |
| $\lambda$, $\beta$ | Longitude–latitude coordinates on planet [Eq. (1)]. |
| $\lambda_0$, $\beta_0$ | Longitude and latitude of optic axis intercept on planet (Fig. 1B). |
| $\omega$, $\omega'$ | Angles measured on the planet and image plane, respectively, about the optic axis intercept (Fig. 1). |
| $P1$–$P4$ | Transforms from image to planetary coordinate systems [Eq. (2)]. |
| $i$ | Incidence angle, measured from normal to a level surface (Fig. 2A). |
| $i''$ | Incidence angle, measured relative to a sloping surface [Eq. (8)]. |
| $e$ | Viewing or emission angle, mea- |

sured from normal to a level surface (Fig. 2A).

$e''$ Viewing or emission angle, measured from normal to a sloping surface [Eq. (9)].

$g$ Phase angle between $i$ and $e$ (Fig. 2A).

$A$ Spacecraft altitude above planet [Eq. (7)].

$R$ Planetary radius [Eq. (1)].

$*$ Subscript indicating subspacecraft point on planet [Eq. (6)].

$\boxdot$ Subscript indicating subsolar point on planet [Eq. (5)].

$\triangledown$ Subscript indicating location on planet within image field of view [Eq. (5)].

$\phi$ Angle on level planetary surface between the traces of the incident and viewing angles (Fig. 2B).

$\psi$ Angle on a level surface between the trace of the incident ray and the strike of a planetary slope (Fig. 3).

$\theta$ Angle of dip of a planetary slope [Eq. (8)].

$N_{\angle'}$ Angle in image plane clockwise from reference axis (positive $x'$) to north direction (Fig. 3).

$S_{\angle'}$ Angle in image plane clockwise from reference axis to Sun direction (Fig. 3).

$V_{\angle'}$ Angle in image plane clockwise from reference axis to spacecraft direction (Fig. 3).

$\tau$ Atmospheric optical thickness [Eq. (11)].

$I_0$ Observed reflected intensity of planetary surface [Eq. (11)].

$D_0$ Observed reflected intensity expressed as digital image number (DIN) of value 0-255 [Eq. (13)].

$I_1$ Reflected intensity of a level planetary surface [Eq. (13)].

$D_1$ Assumed DIN reflected intensity of a level surface [Eq. (13)].

$I_d$ Diffuse reflected intensity from the atmosphere [Eq. (11)].

$S$ Intensity of solar illumination [Eq. (11)].

$k$ Minnaert exponent [Eq. (10)].

$B$ Brightness coefficient [Eq. (10)].

## COORDINATE SYSTEMS

Picture coordinates ($[x', y']$, in pixels) are defined relative to an origin at the center of a Viking image (index 5; pixel coordinates [602.5,528.5]) with $x'$ positive toward index 6 and $y'$ positive toward index 2 (Fig. 1). Note that the $[x', y']$ coordinates differ from the pixel coordinates $[I, J]$ by translation of origin and reversal of the $y'$ axis relative to $J$. A coordinate system ($[x, y]$, in kilometers) is defined on the planetary surface with an origin at the optic axis intercept (index 5 on picture) and with positive $y$ toward geographic north. For large-scale images, longitude–latitude coordinates ($[\lambda, \beta]$, in radians) are related to the $[x, y]$ coordinates by orthographic projection,

$$x = R \cos \beta \sin \lambda'$$

and

$$y = R \{\cos \beta_0 \sin \beta - \sin \beta_0 \cos \lambda'\},$$

where

$$\lambda' \equiv 2\pi - (\lambda - \lambda_0), \quad (1)$$

$R$ is the planetary radius, and $[\lambda_0, \beta_0]$ are the coordinates of the optic axis intercept. The $[x, y]$ and $[x', y']$ coordinates are related by the linear transformation

$$x = P1\, x' + P2\, y'$$

and

$$y = P3\, x' + P4\, y'. \quad (2)$$

The scale factors $P1$ through $P4$ are estimated by least-squares fit to SEDR listings of $[\lambda, \beta]$ for the four corners of the picture (indices 1, 3, 7, 9).

The angles $\omega$ and $\omega'$ measured clockwise to a point $P$ (or $P'$) from the $y$ and $y'$ axes, respectively (Fig. 1), are related by the transformation

$$\tan \omega = (P1 \sin \omega' + P2 \cos \omega')/(P3 \sin \omega' + P4 \cos \omega'). \quad (3)$$

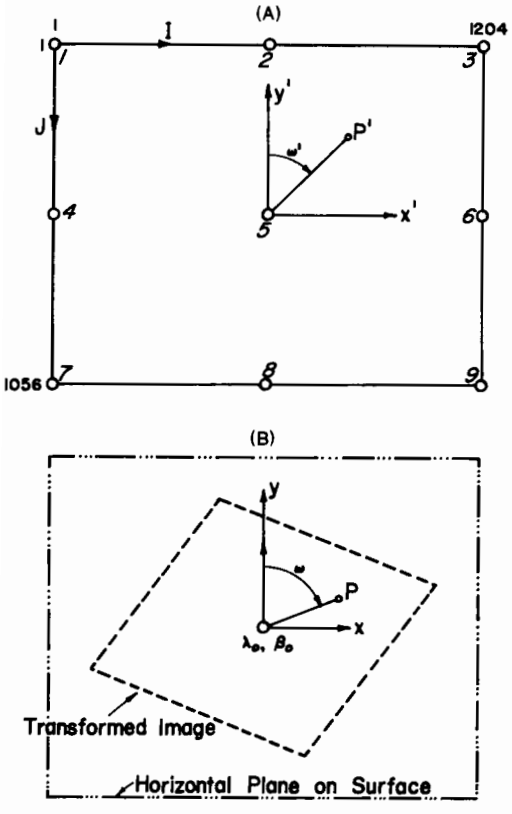


FIG. 1. Coordinate systems on Viking image (A) and planetary surface (B).

## VIEWING GEOMETRY

The angle $\phi$ (Fig. 2B) is related to the angles defining viewing geometry (Fig. 2A) by

$$\cos \phi = (\cos g - \cos i \cos e)/(\sin i \sin e). \quad (4)$$

The following formulas allow calculation of the angles of viewing geometry from information given in SEDR listings. The formulas are from Bonner and Schmall (1973), with minor corrections.

$$\text{Cos } i = \cos \beta_{\boxdot} \cos \beta_{\triangledown} \cos(\lambda_{\boxdot} - \lambda_{\triangledown}) + \sin \beta_{\boxdot} \sin \beta_{\triangledown}, \quad (5)$$

$$\cos g = \{F[\cos \beta_{\boxdot} \cos \beta_* \cos(\lambda_* - \lambda_{\boxdot}) + \sin \beta_{\boxdot} \sin \beta_*] - [\cos \beta_{\boxdot} \cos \beta_{\triangledown} \cos(\lambda_{\triangledown} - \lambda_{\boxdot}) + \sin \beta_{\boxdot} \sin \beta_{\triangledown}]\}/G, \quad (6)$$

$$\cos e = \{F[\cos \beta_{\triangledown} \cos \beta_* \cos(\lambda_* - \lambda_{\triangledown}) + \sin \beta_{\triangledown} \sin \beta_*] - 1\}/G, \quad (7)$$

where

$$F \equiv (1 + A/R),$$

and

$$G \equiv \{F^2 + 1 - 2F [\cos \beta_* \cos \beta_{\triangledown} \cos(\lambda_* - \lambda_{\triangledown}) + \sin \beta_* \sin \beta_{\triangledown}]\}^{1/2}.$$

Using vector geometry it can be shown that the incident and viewing angles on an inclined planetary surface ($i''$ and $e''$) are related to the equivalent angles on a horizontal surface at the same location by

$$\cos i'' = \cos i \cos \theta - \sin i \sin \theta \sin \psi, \quad (8)$$

$$\cos e'' = \cos \psi \sin e \sin \theta \sin \phi - \sin \psi \sin e \sin \theta \cos \phi + \cos e \cos \theta. \quad (9)$$

The angles $N_{\angle'}$, $S_{\angle'}$, and $V_{\angle'}$ (Fig. 3),

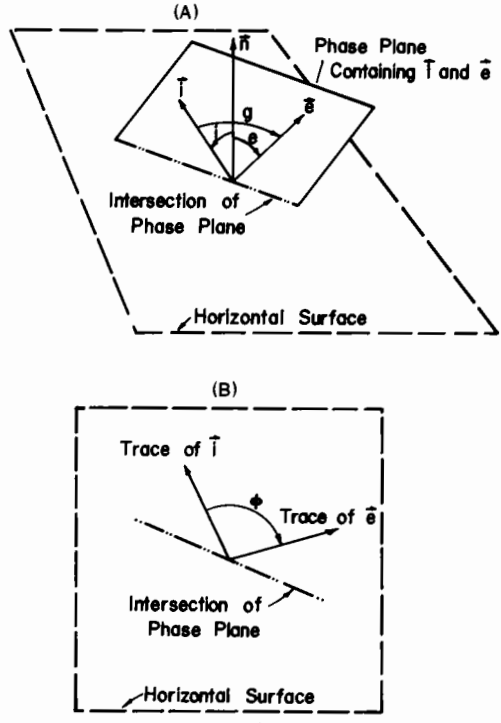


FIG. 2. Definition of viewing and illumination geometry: (A) perspective view; (B) projections on planetary surface.

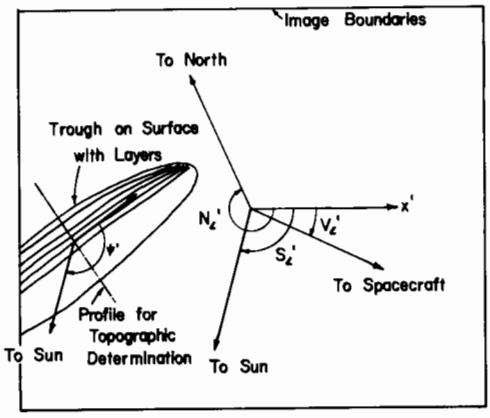


FIG. 3. Angular relationships on Viking image.

which are given in SEDR listings, can be transformed to their equivalent angles on the planetary surface by Eq. (3).

## PHOTOCLINOMETRY

The amount of incident light scattered from a surface depends in general upon the three parameters $i''$, $e''$, and $g$. the most commonly used model photometric function is the Minnaert relationship,

$$P = B\,(\cos i'')^k\,(\cos e'')^{k-1}, \qquad (10)$$

where the parameters $B$ and $k$ are functions of $g$. Veverka (1973) fitted the Minnaert relationship to reflectance measurements made on various ice-, snow-, and frost-covered surfaces by Knowles-Middleton and Mungall (1952). The reflected intensity observed from a spacecraft also depends upon the amount of absorption and reflection within the atmosphere, which is a function of the atmospheric optical depth, $\tau$. The following formula proposed by Pang and Hord (1971) is used to account for atmospheric effects:

$$I_0/S = P\exp\{-\tau(\sec i + \sec e)\} + I_d, \qquad (11)$$

where $I_0/S$ is the observed reflected intensity divided by the intensity of the incident illumination. Diffuse reflection from the atmosphere, $I_d$, is given by

$$I_d = \langle\langle 0.28\cos i\,[1 - \exp\{-\tau(\sec i + \sec e)\}]\rangle\rangle/(\cos i + \cos e). \qquad (12)$$

In order to use photoclinometry the brightness of a level surface at the location in question, measured by the DIN value $D_1$, must be estimated and compared with the actual DIN value, $D_0$. Once estimated, the slope gradient is estimated by finding (iteratively) the gradient value that will satisfy the equation

$$(D_1 S)/I_1 = (D_0 S)/I_0, \qquad (13)$$

where the ratio $I_1/S$ will correspond to substitution in Eq. (10) of $i$ for $i''$ and $e$ for $e''$. The level-surface brightness was generally estimated by assuming that the entire area shown in a Martian polar image had zero average slope, so that, to a first approximation, the value of the left-hand side of Eq. (13) is a constant which can be estimated using the average DIN value for the picture and the central-image values of $i$, $e$, and $g$ [A more accurate approximation would determine the ratio $(D_0S)/I_1$ at each pixel, or for local groups of pixels, and use the average value for the left-hand side of Eq. (13).]

Note from Eqs. (8) and (9) that the values of $e''$ and $i''$ can be estimated only if the strike azimuth of the slope is known. Luckily, much of the topography of the poles consists of long, nearly parallel scarps and troughs. Furthermore, on generally southward-facing scarps many approximately horizontal layers are exposed in cross section. These layers thus are approximate contours that can be used to estimate the slope azimuth. The use of the above equations to estimate slopes is limited to slopes whose strike is appreciably different from the direction of illumination (that is, for cases where $\psi$ is not close to zero). This restriction can be illustrated by assuming that the surface follows a Lambert photometric function ($k$ and $B$ equal unity) and that there are no atmospheric effects ($\tau$ = 0). Then the brightness ratio becomes

$$I_0/I_1 = \cos\theta - \tan i\,\sin\theta\,\sin\psi. \qquad (14)$$

If $\psi$ is near zero, then the brightness ratio is essentially unity for the low-angle polar slopes ($< 10°$), but for values of $\psi$ near 90°, the brightness depends strongly, and nearly linearly, upon the slope angle.

*Effect of Parameter Variation*

Because the determination of slope gradients depends upon accurate estimation of several parameters, it is important to determine the effects that misestimation might have on the generated topographic profiles. Figure 4 illustrates the effect of variation of the main parameters for illumination conditions and slope gradients typical of the north polar data, revealing the following patterns:

1. Estimated slopes are steeper the greater is the assumed atmospheric opacity, but the opacity has little effect for values less than about 0.1 [Fig. 4 (5)].

2. Misestimation of the brightness of a level surface has a strong effect on the shape of the profiles, and can reverse the sense of slope [Fig. 4 (2)]. Surface albedo variations have a similar effect.

3. The photometrically corrected DIN values are presumably absolute in their ratios, so that a ratio of 2 between two DIN values is a correct indicator of their relative brightnesses. Biasing of DIN values has a small effect on estimated slopes, tending to decrease estimates for a positive bias [Fig. 4 (3)].

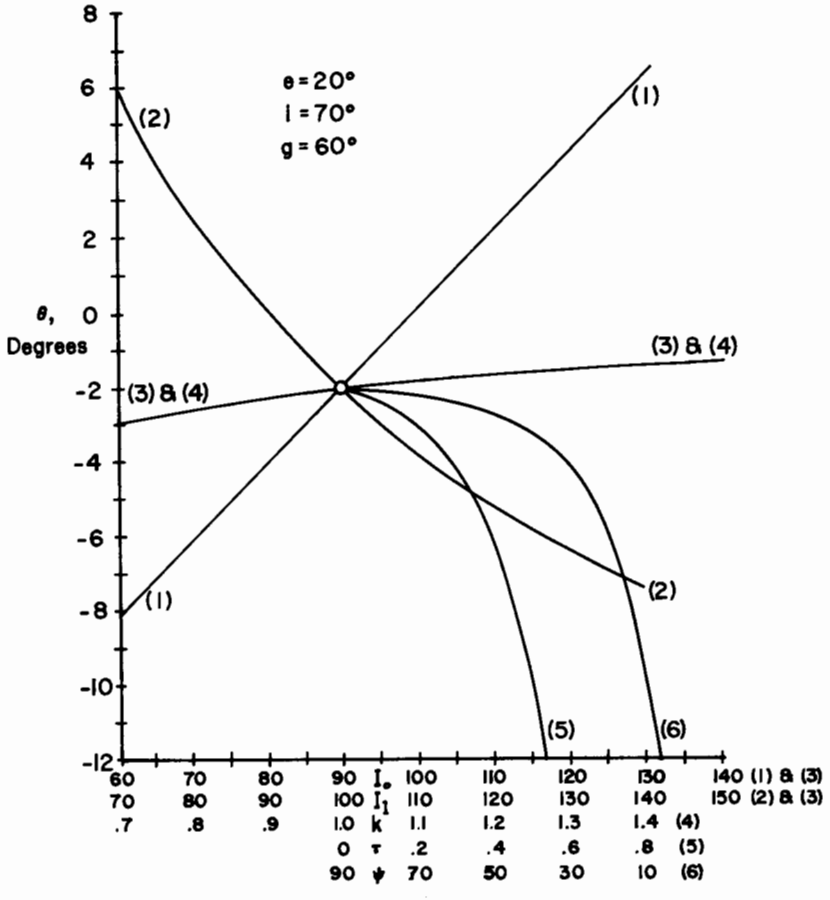


FIG. 4. Effects of parameter variation on estimated surface gradient. Numbered curves reflect effect on calculated slope of independent variations of five parameters as shown below abscissa axis. Parameters $i$, $e$, and $g$ are held constant.

4. The estimated slopes are fairly insensitive to slope orientation error when the azimuths are in the range of 90 ± 45°, but the slope uncertainty increases dramatically for $\psi$ near 0° [Fig. 4 (6)]. This severely limits topographic determination of slopes aligned parallel to the illumination.

5. Variations in the Minnaert parameter $k$ have a small effect upon gradient estimation for a range of 1.0 ± 0.3 [Fig. 4 (4)], and for low atmospheric opacities the parameter $B$ has negligible effect. Data on snow reflectance (Veverka, 1973) and on the brightness of the south polar cap (James *et al.* 1979) suggest values of $k$ for visible light close to unity for the phase angles characteristic of the polar images used here.

Additional complications arise for determination of long topographic profiles in high-altitude images in which appreciable variations in viewing geometry ($i$, $e$, and $g$) occur; however, we have limited the technique to short profiles on large-scale images.

In summary, the technique is rather forgiving of errors in parameters of the photometric function, but is very sensitive to surface albedo variations and to errors in the estimated brightness of a level surface. It is also important to determine whether atmospheric opacity was high enough during acquisition of the spring coverage to affect relief estimates. These potential errors are discussed below in connection with an initial application of the technique to topographic profiling on two Viking images.

## APPLICATION TO VIKING ORBITER IMAGES

Initial tests of the photoclinometric technique used two high-resolution Viking images (566B45 and 566B75) taken during the northern spring ($L_s$ 57°). The viewing geometry is summarized in Table I. These images (Figs. 5 and 6) cover an area near the edge of layered deposits and the perennial polar cap, and the rough-textured terrain (with a few craters) covering portions of the pictures (especially on 566B75) are the "basement" underlying the layered deposits. This exposure of basement is ideal for testing purposes, for these areas, although locally rougher than the polar deposits, appear to be nearly flat overall, although not necessarily level. In addition, stereoscopic coverage was obtained on this orbit (matching pictures 566B67 and 566B53, respectively) and earlier high-resolution Viking coverage was acquired during the previous summer. Both in stereoscopic viewing and from visual assessment of brightness variations (assuming uniform albedo) the topography of the polar deposits appears to be smooth to gently rolling, with the exception of the step-like expression of the layers on steeper slopes.

Data were taken from digital magnetic tape records of observed intensity values (DIN) for individual pixels of the images (each picture is a matrix of 1204 by 1056 pixels). The data were photometrically corrected to account for known inherent camera effects and were despiked (missing or high-amplitude noise data replaced by interpolation), but not geometrically corrected (which reduces spatial resolution).

TABLE I

GEOMETRIC PARAMETERS FOR VIKING IMAGES 566B45 AND 566B75

| Parameter | 566B45 | 566B75 |
|---|---|---|
| $\lambda_0$ | 348.11 | 332.93 |
| $\beta_0$ | 78.69 | 79.13 |
| $\lambda_*$ | 12.34 | 329.13 |
| $\beta_*$ | 78.08 | 80.26 |
| $\lambda_\odot$ | 51.34 | 52.32 |
| $\beta_\odot$ | 20.82 | 20.82 |
| $N_{\angle}$ | 207.58 | 187.60 |
| $S_{\angle}$ | 94.32 | 91.41 |
| $V_{\angle}$ | 122.68 | 215.88 |
| $R$ | 3376.5 | 3376.2 |
| $A$ | 1670.3 | 2144.1 |
| $e$ (at optic axis intercept) | 14.65 | 3.41 |
| $i$ (at optic axis intercept) | 64.46 | 67.57 |
| $g$ (at optic axis intercept) | 51.67 | 69.57 |
| $P1$ | 0.02038 | 0.00765 |
| $P2$ | 0.03953 | 0.05383 |
| $P3$ | −0.03643 | −0.05135 |
| $P4$ | 0.01979 | 0.00725 |

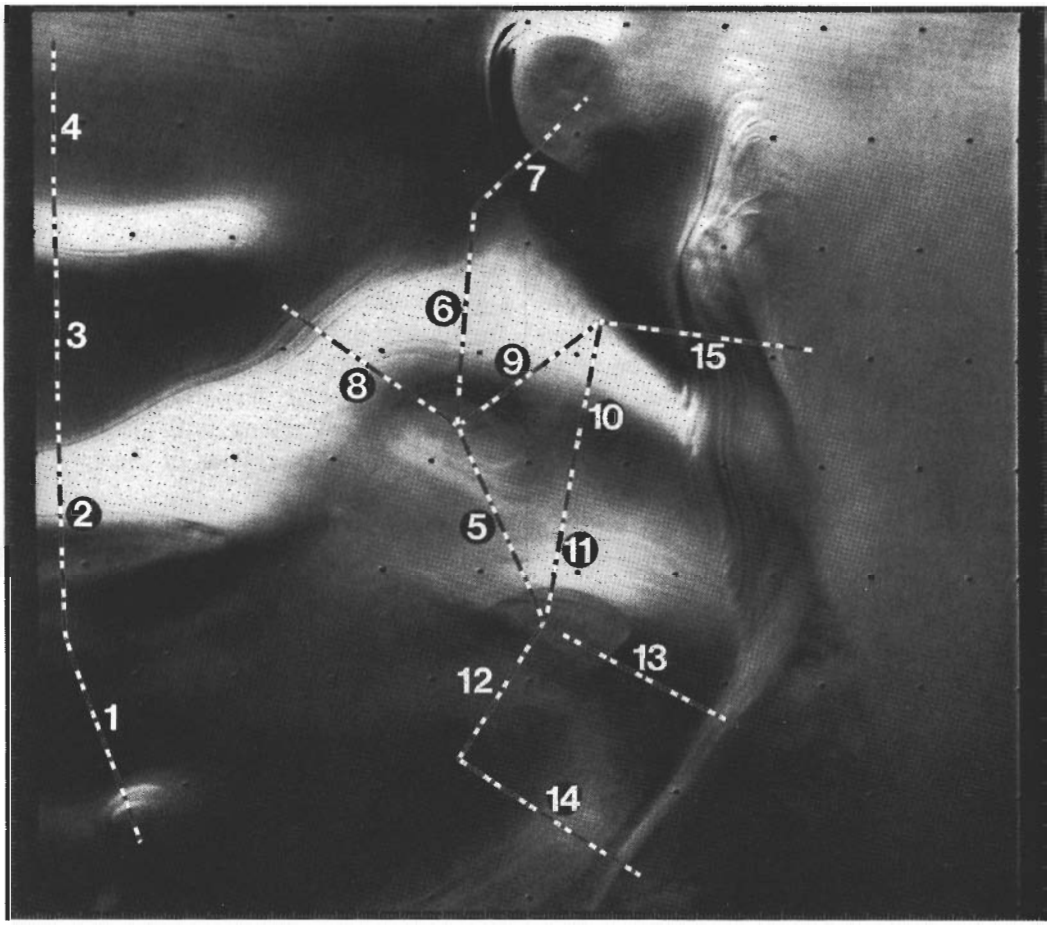


FIG. 5. Photometrically corrected Viking image 566B45, showing location of topographic profiles.

Because the photometric technique is limited to those slopes that have strikes which are known and which are not oriented parallel to the direction of illumination, cross sections may be made only in certain locations and directions. The illumination in both pictures is from the bottom, so that cross sections were concentrated on slopes with left-to-right orientations (Figs. 5 and 6). Computer storage limitations restricted the length of individual cross sections to about 300 pixels, but cross sections were concatenated to give longer profiles.

The first step in producing slope profiles was to specify the pixel coordinates of the start and end of the profile. The strike of the slope relative to the picture axes was visually determined at various points along the profile (Fig. 7A). The strike of outcropping layers was used where these were visible. On smoother slopes, strike azimuth was assumed to run approximately parallel to brightness contours. Between estimation points strike azimuth values were interpolated.

In order to enhance information on the brightness variation across outcropping layers, DINs from pixels lying within a specified range from the cross-section line were combined to produce a brightness profile in the following way.

The cross section was subdivided into subpixel-sized intervals (one to four intervals per pixel). DINs of pixels lying within

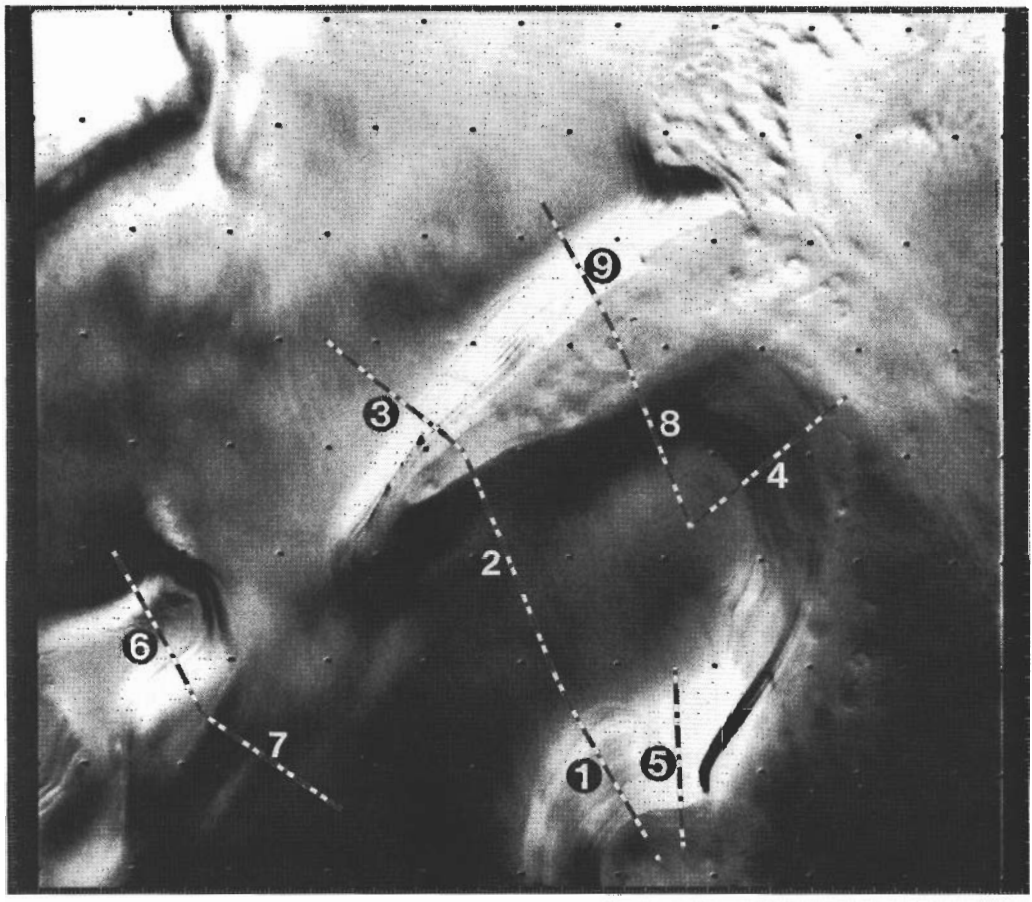


FIG. 6. Photometrically corrected Viking image 566B75, showing location of profiles.

the specified range from the cross section were assigned to the cross-section interval in the direction of the estimated slope strike (Fig. 7B). All brightness values projected to the same interval were combined; the average brightness and standard deviation for each was calculated. Finally, to reduce profile variance and fill in for intervals without pixel contributions, a three-point, 1-2-1 weighted, moving-average filter was used. Weighting was made proportional to the square root of the number of pixels contributing to each interval and to a negative exponential function of the standard deviation.

Experiments were made to select the range and interval length giving the best resolution with the smallest statistical noise (too large a range or too large a box size caused loss of detail). A range value of 4 pixels and two intervals per pixel seemed to give optimum resolution.

The above procedure yielded estimates of the picture brightness and slope azimuth at regularly spaced points along the profile. The final step prior to calculating the slopes was to estimate the brightness corresponding to a level surface at the same location by the technique discussed in the previous section. The first assumption that was made was that the average pixel brightness over the entire picture (neglecting reseau marks) would be a reasonable estimate of level-surface brightness of the picture center. However, it became apparent that there is a brightness trend in the pictures (brighter at

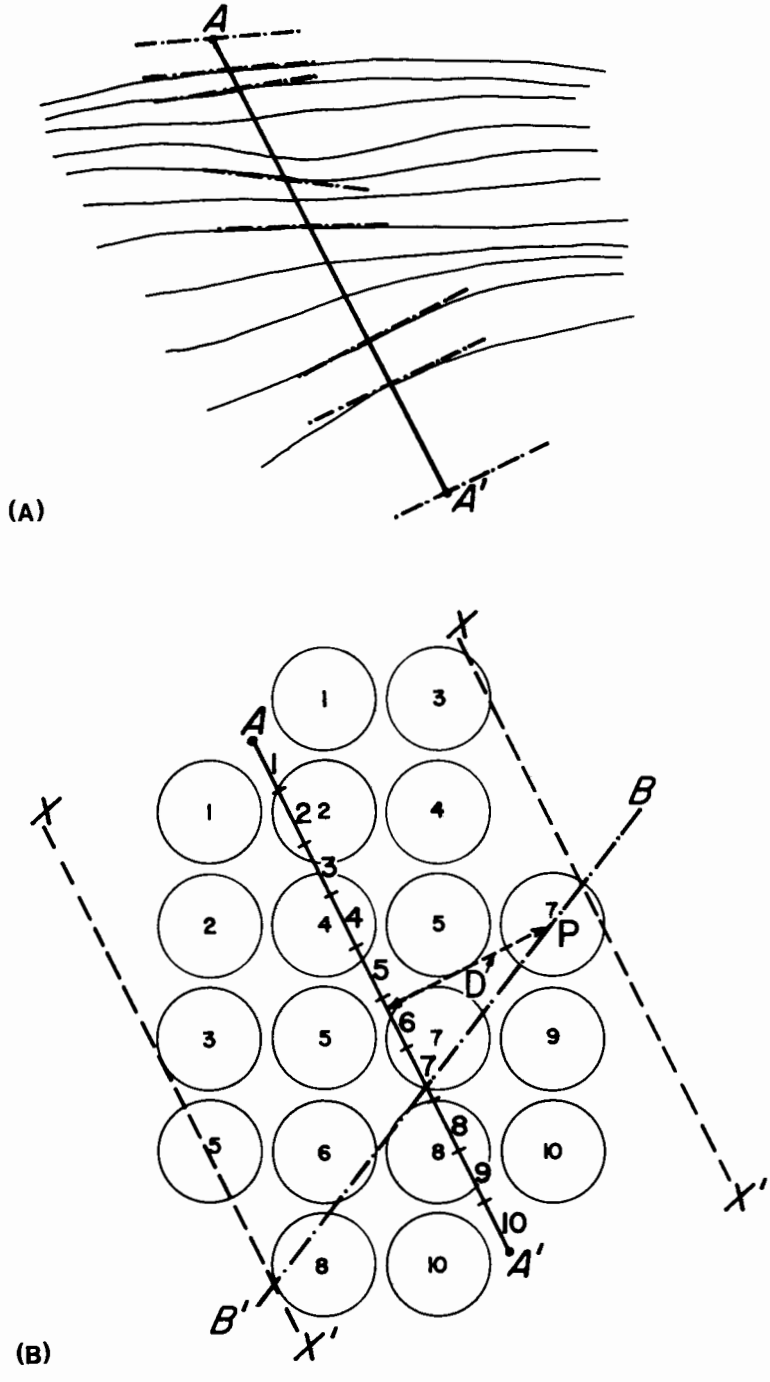


FIG. 7. Brightness profile determination by projection of pixels: (A) Profile ($A$–$A'$) showing individual layers, and estimated strikes (heavy lines); (B) Projection of pixels (circles) into intervals (numbered) on cross section ($A$–$A'$). Line ($B$–$B'$) is estimated surface strike, ($D$) is distance of representative pixel from cross section, and lines ($X$–$X'$) indicate maximum limits of ($D$) for pixel projection. Pixels are labeled by the interval to which they are projected, and noncontributing pixels are omitted.

the top, visible in Figs. 5 and 6) that is several times larger and opposite in sense to the expected brightness variation due to systematic change in viewing geometry across the picture. Although this variation was only about 10% of the average brightness, the profiles did not seem to be realistic. For example, although the basement areas were estimated to be level near the center of the picture, they were noticeably southward sloping at the top and northward sloping at the bottom of the picture. This systematic brightness variation may be a residual camera effect; it was removed in the profiles presented below by fitting a linear trend surface to the brightness values and using the trend surface value as the brightness of the level surface. The trend surfaces for the two images were nearly identical, which suggests that the trends were due to camera effects, particularly in view of the very small variation in viewing geometry across the individual images. For routine use of this method, the photometric properties of the cameras during the time of imaging should be investigated.

Topographic gradients were calculated for each brightness value along the transact using the relationships presented above. In addition to the brightness and slope orientation data, the calculations require specification of the photometric function and the optical thickness of the atmosphere. The topographic profiles presented in Figs. 8 and 9 assume a clear atmosphere and the photometric function was taken from Veverka (1973) for fresh snow. The topographic profile was calculated from the estimated gradients by integration along the profile from an arbitrary datum, with the gradient being corrected by the sine of the acute angle between the profile direction and the slope orientation. Connecting transects were matched at their endpoints.

*Analysis: Consistency and Error*

The profiles generally conform to visual interpretations of the pictures: (1) the topography of the polar deposits is gently rolling, with maximum gradients of a few degrees; (2) the "basement" areas are generally level by comparison with the polar layered deposits; and (3) southward-facing scarps exposing layers are steeper than northward-facing slopes. Self-consistency is indicated by the similar relief estimates given by two transects making different connections between the same endpoints on 566B45 (Fig. 8); the closure error ("X" in the figure) is only about one-tenth of the estimated relief along the two transects.

The two greatest potential sources of error are misestimation of level surface brightness (which tilts the profiles) and unrecognized albedo variations. Because of the potential for systematic bias due to the former cause, the profiles presented here should be considered primarily indicators of relative relief and not as accurate topographic profiles. Comparison with stereo photogrammetric data (Blasius *et al.*, 1982) suggests that the tilt errors are not excessive.

Local variations in surface albedo have been recognized on the two pictures. These are most evident on 566B75 (Fig. 6). Very dark linear zones occur locally on the steep, sunward-facing scarp at the top of the photo. These are probably defrosted zones on particularly steep faces of outcropping layers. In addition, a larger defrosted zone occurs on a steep scarp segment to the lower right. A profile across the scarp near this defrosted zone (number 5 in Figs. 6 and 9) seems exaggerated in relief compared with the nearby profile 1. Around the defrosted zone there occurs a bright halo for a radius of several kilometers. We suspect this may be the result of redeposition of water vapor released from the expanding defrosted zone.

An additional feature raises suspicions of local albedo variations: areas of "basement" that are not interpreted to be flat. The finger of basement extending into the polar deposits in the center of 566B75 (Fig. 6) is indicated to be slightly ridge-like from its photometry. Similarly, the basement ap-

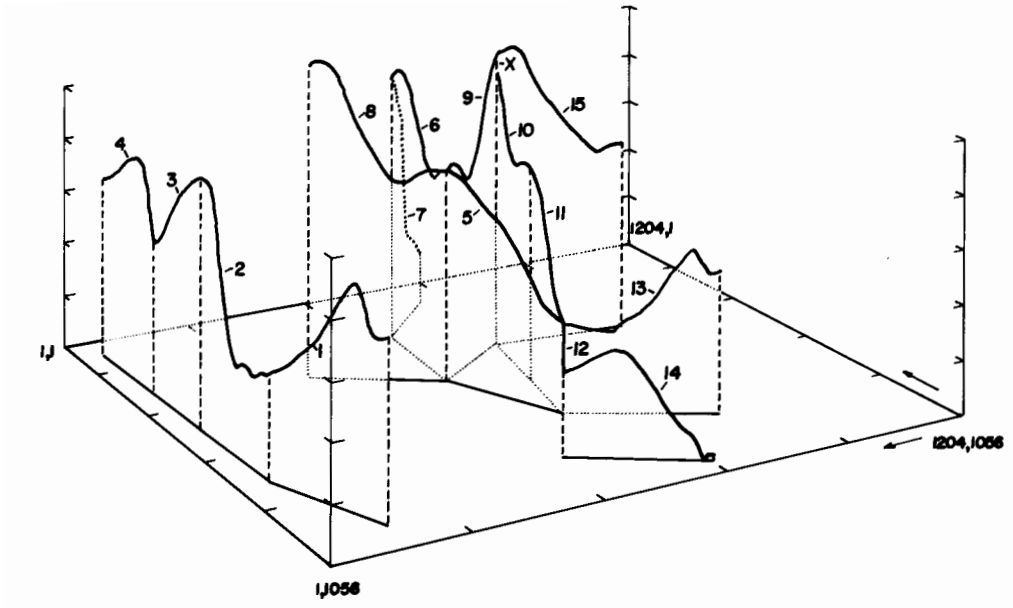


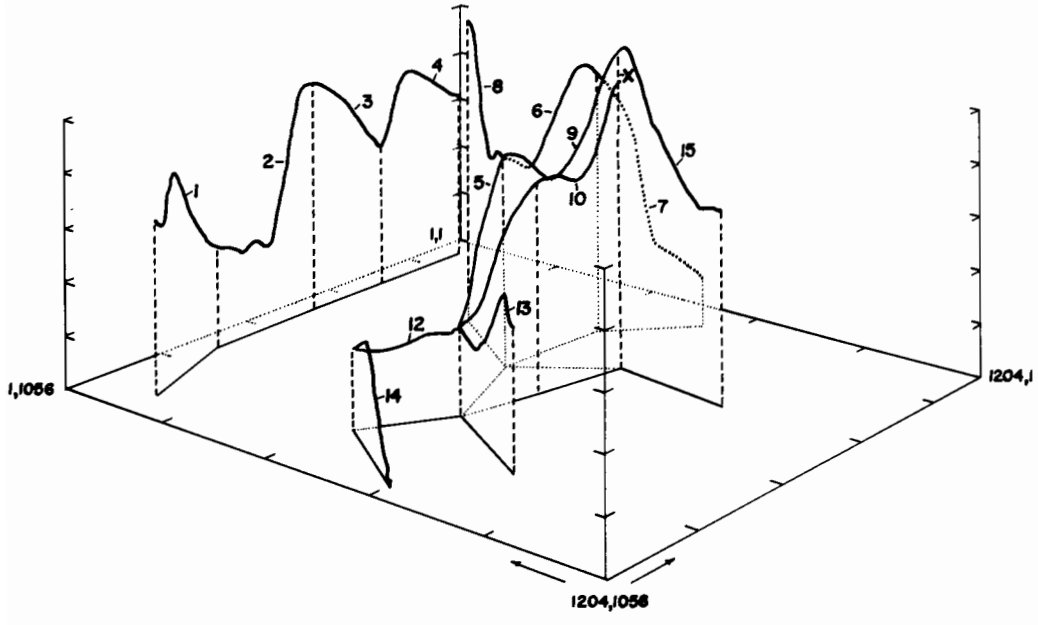


FIG. 8. Perspective views of topographic profiles determined for image 566B45. Angle of view from horizontal = 20°. AV is horizontal counterclockwise rotation of perspective relative to zero for viewing from bottom of image. Elevations of concatenated profiles are matched at their ends, while relative elevations of unconnected profiles are set for qualitative consistency with visual appraisal of topography. Horizontal axes are marked at 10-km intervals from indicated corner. Vertical axes are marked at 200-m intervals. Vertical exaggeration is 20X. See Fig. 5 for key to profiles.

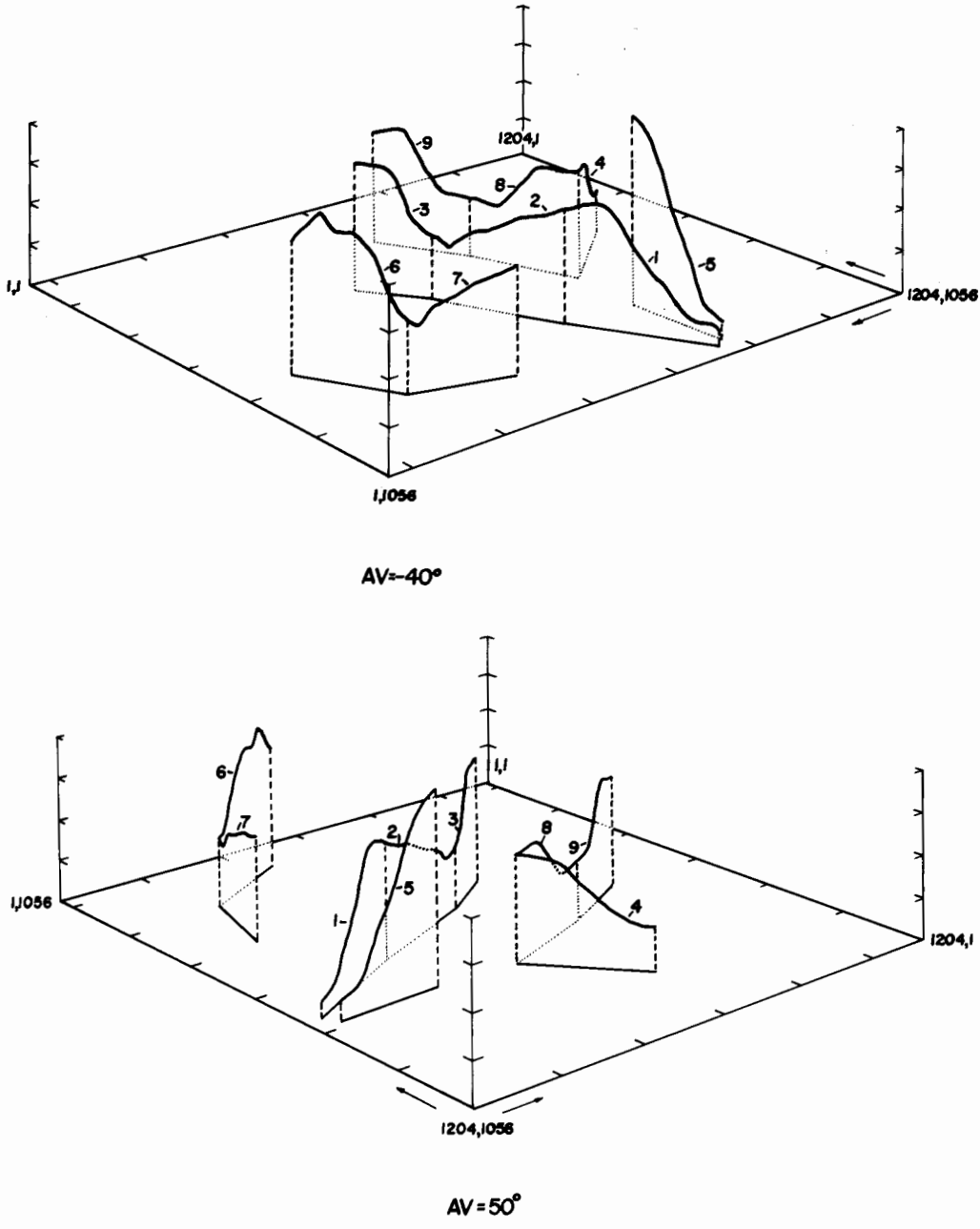


FIG. 9. Perspective views of topographic profiles for 566B75. See Fig. 8 for explanation and Fig. 6 for key to profiles.

pears to have dome-like relief at the end of profile 1 (Fig. 6). A slight brightening of basement plains occurs adjacent to scarps on 566B45 (Fig. 5). Although basement areas are most likely to be exposed where they are highest, the absence of visible large-scale undulations on nearby basement plains suggests that differences in frost thickness or texture cause these apparent relief features. The basement exposed at

the lower end of profile 7 of 566B45 (Fig. 9) is indicated to be appreciably sloping, suggesting either an albedo effect or uncorrected camera effects. Other areas appear to have a more uniform frost cover, but there may be subtle large-scale albedo variations which cause distortions in the profiles. Comparisons with the photogrammetric data (Blasius *et al.*, 1982) again suggest that these are second-order effects.

Cross sections 13 and 14 of 566B45 (Fig. 9) terminate in an exposure of basement that is probably nearly level, but the two cross sections indicate considerably different elevations for the basement. Both the downward trend of profile 14 and the upward trend in profile 15 seem unrealistic. Three sources of error may be involved: residual camera effects, albedo variations, and parameter misestimation on the two profiles. The latter seems to be the most important in this case. Both of these profiles cross terrain that strikes rather close to the illumination angle; under these conditions slight misestimation of topographic strike, when combined with small albedo or camera effects, causes strong distortion of the profiles. Profile 15 on 566B45 and profiles 7 and 4 on 566B75 are suspect for the same reasons, but the indicated relief seems more consistent with visual and stereometric appraisal of the topography.

The existence of appreciable atmospheric opacity may also bias the results of a photoclinometric analysis. The profiles of Figs. 8 and 9 would be underestimates of the true relief, but comparison with photogrammetric data (Blasius *et al.*, 1982) indicates no large atmospheric contribution to scene brightness.

In conclusion, photoclinometry is a valuable tool for determination of relative slopes under conditions where albedo variations are slight, as appears to be the case for spring coverage of the Martian north polar region. Similar techniques might be applied to determination of relief from Landsat photography of terrestrial snow-covered terrains.

ACKNOWLEDGMENTS

This research was supported by NASA Mars Data Analysis Program grants. Digital tapes of corrected images were supplied by the Image Processing Laboratory of the Jet Propulsion Laboratory. The authors are grateful to Ms. Carrington Gregory for conducting the computer analysis.

REFERENCES

BLASIUS, K. R., J. A. CUTTS, AND A. D. HOWARD (1982). Topography and stratigraphy of Martian polar layered deposits. *Icarus* **50,** 139–159.

BONNER, W. J., AND R. A. SCHMALL (1973). A photometric technique for determining planetary slopes from orbital photographs. *US Geol. Surv. Prof. Pap.*, 812-A.

CUTTS, J. A. (1973). Nature and origin of layered deposits of the Martian polar regions. *J. Geophys. Res.* **78,** 4231–4249.

DZURISIN, D., AND K. R. BLASIUS (1975). Topography of the polar layered deposits of Mars. *J. Geophys. Res.* **80,** 3286–3306.

HOWARD, A. D. (1978). Origin of the stepped topography of the Martian poles. *Icarus* **34,** 581–599.

JAMES, P. B., G. BRIGGS, J. BARNES, AND A. SPRUCK (1979). Seasonal recession of Mars' south polar cap as seen by Viking. *J. Geophys. Res.* **84,** 2889–2922.

KNOWLES-MIDDLETON, W. E., AND A. G. MUNGALL (1952). The luminous directional reflectance of snow. *J. Opt. Soc. Amer.* **42,** 572–579.

PANG, K., AND C. W. HORD (1971). Mariner 7 ultraviolet spectrometer experiment: Photometric function and roughness of Mars' polar cap surface. *Icarus* **15,** 443–453.

SQUYRES, S. W. (1981). The topography of Ganymede's grooved terrain. *Icarus* **46,** 156–168.

TOON, O. B., J. B. POLLACK, W. WARD, S. A. BURNS, AND K. BILSKI (1980). The astronomical theory of climatic change on Mars. *Icarus* **44,** 552–607.

VEVERKA, J. (1973). The photometric properties of natural snow and of snow-covered planets. *Icarus* **20,** 304–310.

WARD, W. R., B. C. MURRAY, AND M. C. MALIN (1974). Climatic variations on Mars: Evolution of carbon dioxide atmosphere and polar caps. *J. Geophys. Res.* **79,** 3387–3395.